

A unified equation of state of dense matter and neutron star structure

F. Douchin^{1,2} and P. Haensel³

¹ Department of Physics, University of Illinois at Urbana-Champaign, Urbana, Illinois 61801, USA

² Centre de Recherche Astronomique de Lyon, ENS de Lyon, 69364 Lyon, France

³ N. Copernicus Astronomical Center, Polish Academy of Sciences, Bartycka 18, 00-716 Warszawa, Poland

Received 31 July 2001 / Accepted 10 September 2001

Abstract. An equation of state (EOS) of neutron star matter, describing both the neutron star crust and the liquid core, is calculated. It is based on the effective nuclear interaction SLy of the Skyrme type, which is particularly suitable for the application to the calculation of the properties of very neutron rich matter (Chabanat et al. 1997, 1998). The structure of the crust, and its EOS, is calculated in the $T = 0$ approximation, and under the assumption of the ground state composition. The crust-core transition is a very weakly first-order phase transition, with relative density jump of about one percent. The EOS of the liquid core is calculated assuming (minimal) $n_{pe}\mu$ composition. Parameters of static neutron stars are calculated and compared with existing observational data on neutron stars. The minimum and maximum masses of static neutron stars are $0.094 M_{\odot}$ and $2.05 M_{\odot}$, respectively. Effects of rotation on the minimum and the maximum mass of neutron stars are briefly discussed.

Key words. dense matter – equation of state – stars: neutron

1. Introduction

The equation of state (EOS) of dense neutron star matter is one of the mysteries of these objects. The EOS is a basic input for construction of neutron star models. Its knowledge is needed to calculate the properties of neutron stars, which in turn are necessary for modelling many astronomical objects and phenomena. In particular, the knowledge of the EOS is necessary for the determination of the maximum mass of neutron stars, M_{\max} : compact objects with $M > M_{\max}$ could not be but black holes.

The EOS is predominantly determined by the nuclear (strong) interaction between elementary constituents of dense matter. Even in the neutron star crust, with density below normal nuclear density $\rho_0 = 2.7 \times 10^{14} \text{ g cm}^{-3}$ (corresponding to baryon density $n_0 = 0.16 \text{ fm}^{-3}$), nuclear interactions are responsible for the properties (and actually – for the very existence!) of neutron rich nuclei, crucial for the crust EOS. The knowledge of these interactions is particularly important for the structure of the inner neutron star crust, where nuclei are immersed in a neutron gas, and even more so for the EOS of the liquid core. Nuclear interactions are actually responsible for a dramatic lifting of M_{\max} from $0.7 M_{\odot}$, obtained when interactions are switched-off (Oppenheimer & Volkoff 1939), above measured $1.44 M_{\odot}$ of PSR B1913+16, and maybe even above $2 M_{\odot}$, as suggested by some models of the kHz

quasi periodic oscillations in 4U 1820-30 (Zhang et al. 1997; Miller et al. 1998; Kluźniak 1998).

The outer envelope of a neutron star with $\rho < \rho_0$ contains the same elementary constituents as ordinary (e.g. terrestrial) matter, i.e., protons, neutrons, and electrons. Unfortunately, even within this subnuclear density envelope, calculation of the EOS starting from an experimentally determined *bare* nucleon-nucleon (NN) interaction *in vacuum*, supplemented with a three-nucleon (NNN) force (which is necessary to fit the properties of ^3H and ^4He simultaneously with the two body data), is not feasible. This is due to the prohibitive complexity of the many-body problem to be solved in the case of heavy nuclei (more generally: for nuclear structures – spheres, rods, plates etc. Lorenz et al. 1993) immersed in a neutron gas. To make a calculation feasible, one uses a mean field approximation with an *effective* NN interaction, an approach used with great success in terrestrial nuclear physics. The most ambitious application of this approach to the determination of the structure and EOS of the neutron star crust remains the classical work of Negele & Vautherin (1973). Other authors, who treated this problem, used additional approximations of the quantum mean-field scheme (see: Oyamatsu 1993; Lorenz et al. 1993; Sumiyoshi et al. 1995; Cheng et al. 1997; Douchin & Haensel 2000, and references therein).

It is clear that in order to describe in a physically (in particular, thermodynamically) consistent way both the crust, the liquid core, and the transition between them,

Send offprint requests to: P. Haensel,
e-mail: haensel@camk.edu.pl

one has to use the same many-body model and the same effective NN interaction, on both sides of the crust-core interface. The mean-field scheme can also be applied for the description of the spatially uniform npe liquid provided one uses appropriate effective NN interaction. Note that in this case the calculation of the ground state of nucleon matter can be done also, with rather high precision (at not too high density), starting with bare nuclear Hamiltonian \hat{H}_N (resulting from bare NN and NNN interactions) (Wiringa et al. 1988; Akmal et al. 1998). The calculated ground state energy $\langle \Psi_0 | \hat{H}_N | \Psi_0 \rangle$ (here Ψ_0 is the actual ground state wave function, which includes nucleon correlations, and minimizes the energy of the system) has then to be approximated, as well as possible, by $\langle \Phi_0 | \hat{H}_N^{\text{eff}} | \Phi_0 \rangle$, where Φ_0 is the Hartree-Fock wave function, and \hat{H}_N^{eff} is effective nuclear Hamiltonian.

Some authors formulated the nuclear many-body problem, relevant for neutron star matter, within relativistic mean-field models, in which nuclear interactions are described by a phenomenological Lagrangian involving coupling of the nucleon fields to the meson fields (Sumiyoshi et al. 1995; Cheng et al. 1997). While such an approach has an obvious advantage at very high density (it yields causal EOS, by construction), its meaning at lower densities is not clear (see, e.g., Heiselberg & Pandharipande 2000). In the present paper we restrict ourselves to the non-relativistic approach.

Once the many-body approximation was fixed, the input consists of the effective NN interaction, which has to reproduce a wealth of experimental data on atomic nuclei, especially those with high neutron excess, as well as reproduce the most reliable numerical results concerning the ground state of dense homogeneous neutron rich nucleon matter. In the case of the calculation of the EOS of neutron star matter, the latter condition may be reduced to the limiting case of pure neutron matter; as it turns out, in such a case many-body calculations with a bare nucleon Hamiltonian are particularly precise, mostly because of the less important role played by the tensor forces (Wiringa et al. 1988).

An effective nucleon Hamiltonian contains a number of parameters which are usually fixed by fitting experimental data on saturation properties of bulk nuclear matter and experimental properties of selected atomic nuclei. The parameters of \hat{H}_N^{eff} are also constrained by some general condition, e.g., of spin stability (Kutschera & Wójcik 1994). Most of the existing effective interactions were fitted to the properties of laboratory atomic nuclei, with $(N - Z)/A < 0.3$, while in the bottom layers of the neutron-star crust, and even more so in the liquid core, one expects $(n_n - n_p)/n_b \gtrsim 0.8$. In view of this, application of these effective nuclear interactions to neutron star interior involves a rather risky extrapolation to strongly asymmetric nucleon matter. In order to remove a part of this uncertainty, modifications of effective nuclear forces, to make them consistent with available (and possibly reliable) results of microscopic calculations of neutron

matter, have been applied. Such a procedure was used in the seventies to obtain the Sk1' force (Lattimer & Ravenhall 1978), via a rather ad hoc modification of the Sk1 force constructed originally by Vautherin and Brink (Vautherin & Brink 1970) to describe terrestrial nuclei. In this way, Sk1' became consistent with energy per nucleon of neutron matter calculated by Siemens & Pandharipande (1971). Later, generalized types of the Skyrme interaction, FPS (Pandharipande & Ravenhall 1989) and FPS21 (Pethick et al. 1995), with a larger number of fitted parameters and more general density dependence, were derived by fitting the temperature and baryon density dependent energies per baryon of nuclear and neutron matter obtained in microscopic calculations of Friedman & Pandharipande (1981).

A new set of the Skyrme-type effective N-N interactions has been derived recently, based on an approach which may be more appropriate, as far as the applications to a very neutron rich matter are concerned (Chabanat et al. 1997; Chabanat et al. 1998). While being of a two-body type, this effective interaction contains, in the spirit of the Skyrme model, a term resulting from averaging of an original three-body component. Relevant additional experimental items concerning neutron rich nuclei (including isovector effective masses), constraints of spin stability and requirement of consistency with the UV14+VIII equation of state (EOS) of dense neutron matter of Wiringa et al. (1988) for $n_0 \leq n_b \leq 1.5 \text{ fm}^{-3}$ were combined with the general procedure of fitting the properties of doubly magic nuclei. This procedure led to a set of the SLy (**S**kyrme **L**yon) effective nucleon-nucleon interactions which – due to the emphasis put on their neutron-excess dependence – seem to be particularly suitable for the calculations of the properties of neutron-star interiors. The FPS force was constructed as a generalized Skyrme model, by fitting the properties of asymmetric dense, cold and hot, nucleon matter, calculated by Friedman & Pandharipande (1981); fitting of the ground state properties of laboratory nuclei was not included in their derivation. Luckily, the FPS force turned out to reproduce rather well, without additional adjustment, the ground state energies of eight doubly closed-shell nuclei ranging from ^{16}O to ^{208}Pb (Lorenz et al. 1993).

The SLy forces have been constructed so as to be consistent with the UV14+UVII model of Wiringa et al. (1988) of neutron matter *above* n_0 (Chabanat et al. 1997; Chabanat et al. 1998). It is therefore of interest to check how well these effective N-N interactions reproduce the UV14+UVII equation of state of neutron matter at subnuclear densities. This feature is quite important for the correct calculation of the equation of state of the bottom layers of neutron star crust and of the liquid core, which contain only a few percent of protons. We do not have direct access to the “experimental equation of state” of pure neutron matter at subnuclear densities. However, results of the best numerical many-body calculations of the ground state of neutron matter with realistic \hat{H}_N seems to be sufficiently precise at subnuclear densities to be used

as an *ersatz* of experimental data (Pethick et al. 1995). The SLy effective interaction passes this test very well, in contrast to most of other models of \hat{H}_N^{eff} (Douchin & Haensel 2000). In what follows, by the SLy interaction we will mean the basic SLy4 model of Chabanat et al. (1998).

After our unified EOS was constructed, a new state-of-the-art microscopic calculation of the EOS of dense matter (Akmal et al. 1998), which in many respect is superior to the ten years older models of Wiringa et al. (1988), became available. The nuclear Hamiltonian of Akmal et al. (1998) is based on a new Argonne two-nucleon interaction AV18, takes into account relativistic boost corrections to the two-nucleon interaction, and includes new Urbana model of three-nucleon interaction, UIX. In what follows, the most complete models of the EOS of dense cold catalyzed matter, AV18 + δv + UIX*, calculated by Akmal et al. (1998), will be referred to as APR (Akmal Pandharipande Ravenhall). It should be stressed, that in contrast to the FPS and SLy EOS, the APR EOS describes only the liquid core of neutron star, and therefore is not a “unified EOS” of the neutron star interior. As we will show, neutron star models based on the APR EOS of the liquid core, supplemented with our EOS of the crust, are not very different from the stellar models calculated using our complete, unified EOS.

In the present paper we calculate the unified EOS for neutron star matter using the SLy effective NN interaction. Nuclei in the crust are described using the Compressible Liquid Drop Model, with parameters calculated using the many-body methods presented in Douchin et al. (2000) and Douchin & Haensel (2000). The calculation of the EOS is continued to higher densities, characteristic of the liquid core of neutron star. Using our EOS, we then calculate neutron star models and compare their parameters with those obtained using older FPS effective NN interaction. We consider also effects of rotation on neutron star structure. Our neutron star models are then confronted with observations of neutron stars.

The method of the calculation of the EOS for the crust and the liquid core of neutron star is described in Sect. 2. Results for the structure and the EOS of the crust are given in Sect. 3, and those for the liquid core in Sect. 4. Models of neutron stars are reviewed in Sect. 6. Effects of rotation on neutron star structure are briefly discussed in the two last subsections of Sect. 6. Comparison with observations of neutron stars is presented in Sect. 7. Finally, Sect. 8 contains summary and conclusion of our paper.

2. Method of solution of the many-body problem

2.1. The crust

Nuclei in the neutron-star crust are described using the Compressible Liquid Drop Model (CLDM) of nuclei (Douchin et al. 2000 and references therein). The parameters of the model are calculated using the SLy effective interaction. Within the CLDM, one is able to separate bulk, surface and Coulomb contributions to total energy

density, E . Electrons are assumed to form a uniform Fermi gas and yield the rest plus kinetic energy contribution, denoted by E_e . Total energy density of the neutron-star crust is given by

$$E = E_{N, \text{bulk}} + E_{N, \text{surf}} + E_{\text{Coul}} + E_e. \quad (1)$$

Here, $E_{N, \text{bulk}}$ is the bulk contribution of nucleons, which does not depend on the shape of nuclei. However, both $E_{N, \text{surf}}$ and E_{Coul} do depend on this shape. Actually, in the case of the bottom layers of the inner crust, one has to generalize the notion of “nuclei” to “nuclear structures” formed by denser nuclear matter and the less dense neutron gas. Detailed description of the calculation of $E_{N, \text{surf}}$ and E_{Coul} for the SLy forces was presented in Douchin (1999) and Douchin et al. (2000). Its application to the calculation of the properties of the inner crust is presented in Douchin & Haensel (2000). We restricted ourselves to three shapes of the nuclear matter – neutron gas interface: spherical, cylindrical, and plane. Consequently, we considered five types of nuclear structures: spheres of nuclear matter in neutron gas, cylinders of nuclear matter in neutron gas (rods), plane slabs of nuclear matter in neutron gas, cylindrical holes in nuclear matter filled by neutron gas (tubes) and spherical holes in nuclear matter filled by neutron gas (bubbles). In view of a significant neutron excess, the interface includes neutron skin formed by neutrons adsorbed onto the nuclear matter surface. In view of a finite thickness of nuclear surface, the definition of its spatial location is a matter of convention. Here, we defined it by the radius of the equivalent constant density proton distribution, R_p , which determines thus the radius of spheres, bubbles, cylinders and tubes, and the half-thickness of plane nuclear matter slabs. The neutron radius, R_n , was defined by the condition that it yields a squared-off neutron density distribution with constant neutron densities, which are equal to the real ones far from the nuclear matter – neutron gas interface, and reproduces actual total number of neutrons. The thickness of the neutron skin was then defined as $R_n - R_p$. The nuclear surface energy term, $E_{N, \text{surf}}$, gives the contribution of the interface between neutron gas and nuclear matter; it includes contribution of neutron skin (Pethick & Ravenhall 1995; Lorenz 1991). In the case of spherical and cylindrical interface, $E_{N, \text{surf}}$ includes curvature correction; the curvature correction vanishes for slabs.

In order to calculate E_{Coul} , we used the Wigner-Seitz approximation. In the case of spheres, bubbles, rods and tubes, Wigner-Seitz cells were approximated by spheres and cylinders, of radius R_{cell} . In the case of slabs, Wigner-Seitz cells were bounded by planes, with R_{cell} being defined as the half-distance between plane boundaries of the cell. At given average nucleon (baryon) density, n_b , and for an assumed shape of nuclear structures, the energy density was minimized with respect to thermodynamic variables, under the condition of an average charge neutrality. Spherical nuclei are energetically preferred over other nuclear shapes, and also over homogeneous npe matter, down to $n_{\text{edge}} = 0.076 \text{ fm}^{-3}$. Within our set of possible

nuclear shapes therefore, the ground state of neutron-star crust contains spherical nuclei only. A detailed study of the bottom layers of the inner crust, including the determination of its bottom edge, is presented in Douchin & Haensel (2000).

2.2. The liquid core

For $n_{\text{edge}} < n_{\text{b}} < 2n_0$ neutron star matter is expected to be a homogeneous plasma of neutrons, protons and electrons, and – above the threshold density for the appearance of muons (when electron chemical potential $\mu_e > m_\mu c^2 = 105.7$ MeV) – also negative muons. Such a npe μ model of dense matter is expected to be valid at not too a high density (say, $n \lesssim 3n_0$). At still higher densities one may contemplate possibility of the appearance of hyperons. However, in view of a lack of detailed knowledge of the hyperon-nucleon and hyperon-hyperon interactions, we prefer to extrapolate the npe μ model to higher densities (this is the approach used also in Wiringa et al. 1988, and in more recent calculation of Akmal et al. 1998).

The total energy density of the npe μ matter, E (which includes rest energy of matter constituents), is a sum of the nucleon contribution, $E_{\text{N}}(n_{\text{n}}, n_{\text{p}})$, and of the lepton one. We have

$$E(n_{\text{n}}, n_{\text{p}}, n_{\text{e}}, n_{\mu}) = E_{\text{N}}(n_{\text{n}}, n_{\text{p}}) + n_{\text{n}}m_{\text{n}}c^2 + n_{\text{p}}m_{\text{p}}c^2 + E_{\text{e}}(n_{\text{e}}) + E_{\mu}(n_{\mu}) \quad (2)$$

where E_{e} , E_{μ} are the energy densities, and n_{e} and n_{μ} are number densities of electrons and muons respectively. Coulomb contributions are negligible compared to the kinetic energies of leptons and therefore they can be treated as free Fermi gases. Mass density of matter is $\rho = E/c^2$.

The equilibrium of the npe μ matter with respect to weak interactions implies relations involving chemical potentials of matter constituents,

$$\mu_{\text{n}} = \mu_{\text{p}} + \mu_{\text{e}}, \quad \mu_{\mu} = \mu_{\text{e}} \quad (3)$$

where

$$\mu_j = \frac{\partial E}{\partial n_j}, \quad j = \text{n, p, e, } \mu. \quad (4)$$

At given $n_{\text{b}} = n_{\text{n}} + n_{\text{p}}$, charge neutrality, $n_{\text{p}} = n_{\text{e}} + n_{\mu}$, combined with Eq. (3), yield the equilibrium fractions $x_j = n_j/n_{\text{b}}$. Using then Eq. (2), one calculates the equilibrium (ground-state) value of $E(n_{\text{b}})$ (minimum E at given n_{b}). This gives a one-parameter EOS of npe μ matter,

$$\rho(n_{\text{b}}) = \frac{E(n_{\text{b}})}{c^2}, \quad P(n_{\text{b}}) = n_{\text{b}}^2 \frac{d}{dn_{\text{b}}} \left(\frac{E(n_{\text{b}})}{n_{\text{b}}} \right). \quad (5)$$

3. Structure and equation of state of the crust

3.1. The outer crust

Our calculations have been limited to $\rho > 10^6$ g cm $^{-3}$. The neutron star envelope with $\rho < 10^6$ g cm $^{-3}$ has a

tiny mass $\sim 10^{-10} M_{\odot}$, and moreover its composition and structure can be influenced by various factors, such as accretion of interstellar matter, and/or the presence of strong magnetic field¹.

One has to be aware of the simplifications and approximations inherent to the CLDM. While the parameters of this model are determined in quantum-mechanical many-body calculation, the model itself is *par excellence* classical. It does not exhibit therefore the *shell effects* corresponding to the closure of proton or neutron shells in nuclei or the effect of neutron or proton pairing. Shell effects imply particularly strong binding of nuclei with “magic numbers” of $Z = 28$ and $N = 50, 82$. Consequently (except at lowest density) nuclei present in the ground state of outer crust are expected to have $Z = 28$ (at lower density) or $N = 50, 82$ (at higher density) (Baym et al. 1971b; Haensel & Pichon 1994). This feature is absent in the CLDM EOS, which additionally treats Z and A as continuous variables. As a result, CLDM EOS at $\rho < \rho_{\text{ND}}$ is *softer* and has lower value of neutron drip density (real nuclei are stabilized against neutron drip by the pairing and the shell effects for neutrons) than that based on experimental nuclear masses.

Actually, for $\rho \lesssim 10^{11}$ g cm $^{-3}$, the EOS of the ground state of the outer crust can be reliably determined using *experimental* masses of neutron-rich nuclei (Haensel & Pichon 1994). The last “experimental” nucleus present in the ground state of the outer crust is doubly magic ^{78}Ni ($N = 50, Z = 28$), with proton fraction $Z/A = 0.36$. Then, up to neutron drip density, the EOS can be quite reliably determined using the extrapolation of nuclear masses, beyond the experimentally available region, via semiempirical nuclear mass formulae (Haensel & Pichon 1994). Within such an approach, which makes maximal use of experimental nuclear data, neutron drip takes place at 4.3×10^{11} g cm $^{-3}$ and for $Z/A = 0.30$. In view of this, we suggest to replace, in neutron star calculations, the SLy EOS at $\rho < \rho_{\text{ND}} = 4.3 \times 10^{11}$ g cm $^{-3}$ by that of Haensel & Pichon (1994), and to match it with the SLy EOS for the inner crust above ρ_{ND} . This is what we did in our calculations of neutron star structure.

3.2. The inner crust

The values of A, Z , fraction of nucleons in neutron gas outside nuclei, and geometrical parameters characterizing lattice of nuclei in the inner crust are displayed in Tables 1, 2. The crust-liquid core transition takes place not because nuclei grow in size but rather because they become closer and closer. The filling fraction u grows rapidly for n_{b} approaching n_{edge} from only 5% at $n_{\text{b}} = 0.04$ fm $^{-3}$ to nearly 30% at the bottom edge. Still, less than 30% of

¹ A more precise condition for the degenerate neutron star envelope to be unaffected by the magnetic field is $\rho > 2.2 \times 10^5 (A/Z)(B/10^{13} \text{ G})^{3/2}$ g/cm 3 , where A and Z are mass number and atomic number of the nuclei in the plasma (Yakovlev & Kaminker 1994).

Table 1. Structure and composition of the inner neutron-star crust (ground state) calculated within the Compressible Liquid Drop Model with SLy effective nucleon-nucleon interaction. X_n is the fraction of nucleons in the neutron gas outside nuclei. Upper part with $X_n = 0$ corresponds to a shell of the outer crust, just above the neutron drip surface in the neutron-star interior, and calculated within the same model. The equivalent proton and neutron radii, R_p and R_n , are defined in the text. Wigner-Seitz cell radius and fraction of volume occupied by nuclear matter (equal to that occupied by protons) are denoted by R_{cell} and u , respectively.

n_b (fm^{-3})	Z	A	X_n	R_p (fm)	R_n (fm)	R_{cell} (fm)	u (%)
1.2126 E-4	42.198	130.076	0.0000	5.451	5.915	63.503	0.063
1.6241 E-4	42.698	135.750	0.0000	5.518	6.016	58.440	0.084
1.9772 E-4	43.019	139.956	0.0000	5.565	6.089	55.287	0.102
2.0905 E-4	43.106	141.564	0.0000	5.578	6.111	54.470	0.107
2.2059 E-4	43.140	142.161	0.0247	5.585	6.122	54.032	0.110
2.3114 E-4	43.163	142.562	0.0513	5.590	6.128	53.745	0.113
2.6426 E-4	43.215	143.530	0.1299	5.601	6.145	53.020	0.118
3.0533 E-4	43.265	144.490	0.2107	5.612	6.162	52.312	0.123
3.5331 E-4	43.313	145.444	0.2853	5.623	6.179	51.617	0.129
4.0764 E-4	43.359	146.398	0.3512	5.634	6.195	50.937	0.135
4.6800 E-4	43.404	147.351	0.4082	5.645	6.212	50.269	0.142
5.3414 E-4	43.447	148.306	0.4573	5.656	6.228	49.615	0.148
6.0594 E-4	43.490	149.263	0.4994	5.667	6.245	48.974	0.155
7.6608 E-4	43.571	151.184	0.5669	5.690	6.278	47.736	0.169
1.0471 E-3	43.685	154.094	0.6384	5.725	6.328	45.972	0.193
1.2616 E-3	43.755	156.055	0.6727	5.748	6.362	44.847	0.211
1.6246 E-3	43.851	159.030	0.7111	5.784	6.413	43.245	0.239
2.0384 E-3	43.935	162.051	0.7389	5.821	6.465	41.732	0.271
2.6726 E-3	44.030	166.150	0.7652	5.871	6.535	39.835	0.320
3.4064 E-3	44.101	170.333	0.7836	5.923	6.606	38.068	0.377
4.4746 E-3	44.155	175.678	0.7994	5.989	6.698	36.012	0.460
5.7260 E-3	44.164	181.144	0.8099	6.059	6.792	34.122	0.560
7.4963 E-3	44.108	187.838	0.8179	6.146	6.908	32.030	0.706

the volume is filled by nuclear matter at the crust-liquid core transition point. Finally, let us mention that no proton drip occurs in the ground state of the crust.

As we see in Tables 1 and 2, the number of nucleons in a nucleus, A , grows monotonically with increasing density and reaches about 600 at the edge of the crust. However, the number of protons changes rather weakly, from $Z \simeq 40$ near neutron drip, to $Z \simeq 50$ near the edge of the crust. Our results for Z of spherical nuclei are similar to those obtained in Ravenhall et al. (1972) and Oyamatsu (1993), but are somewhat higher than those obtained using a relativistic mean-field model in Sumiyoshi et al. (1995). The problem of stability of nuclei in the bottom layer of the inner crust with respect to fission was discussed in Douchin & Haensel (2000).

Actually, under conditions of thermodynamic equilibrium, transition from the crust to the uniform liquid takes place at a constant pressure, and is accompanied by a density jump (first order phase transition). Using Maxwell construction, we find that the edge of the crust has density $n_{\text{edge}} = 0.076 \text{ fm}^{-3}$, and coexists there with uniform npe matter of the density higher by $\Delta\rho/\rho_{\text{edge}} \simeq \Delta n_b/n_{\text{edge}} = 1.4\%$. Crust-liquid core transition is

therefore a very weak first-order phase transition; it takes place at $P_{\text{edge}} = 5.37 \times 10^{32} \text{ erg cm}^{-3}$.

4. Composition and equation of state of neutron star core

Composition of the liquid core is given in Table 4. Muons appear at $n_b = 0.12 \text{ fm}^{-3}$. Particularly important for the rate of the neutron star cooling is the relation between x_n and x_p , x_e , and x_μ . Namely, the powerful direct Urca process of neutrino emission, $n \rightarrow p + e + \bar{\nu}_e$, $p + e \rightarrow n + \nu_e$, is allowed only if the values of the Fermi momenta in the npe μ matter satisfy the ‘‘triangle condition’’ $p_{F_n} < p_{F_p} + p_{F_e}$. Similarly, direct Urca process involving muons, $n \rightarrow p + \mu^- + \bar{\nu}_\mu$, $p + \mu^- \rightarrow n + \nu_\mu$, is allowed only if $p_{F_n} < p_{F_p} + p_{F_\mu}$ (Lattimer et al. 1991). The ‘‘triangle conditions’’ can be expressed in terms of the particle fractions x_j as

$$\text{electron direct Urca: } x_n^{\frac{1}{3}} < x_p^{\frac{1}{3}} + x_e^{\frac{1}{3}},$$

$$\text{muon direct Urca: } x_n^{\frac{1}{3}} < x_p^{\frac{1}{3}} + x_\mu^{\frac{1}{3}}, \quad (6)$$

Table 2. Structure and composition of the inner neutron-star crust – continued. Last line corresponds to the bottom edge of the inner crust.

n_b (fm^{-3})	Z	A	X_n	R_p (fm)	R_n (fm)	R_{cell} (fm)	u (%)
9.9795 E-3	43.939	195.775	0.8231	6.253	7.048	29.806	0.923
1.2513 E-2	43.691	202.614	0.8250	6.350	7.171	28.060	1.159
1.6547 E-2	43.198	211.641	0.8249	6.488	7.341	25.932	1.566
2.1405 E-2	42.506	220.400	0.8222	6.637	7.516	24.000	2.115
2.4157 E-2	42.089	224.660	0.8200	6.718	7.606	23.106	2.458
2.7894 E-2	41.507	229.922	0.8164	6.825	7.721	22.046	2.967
3.1941 E-2	40.876	235.253	0.8116	6.942	7.840	21.053	3.585
3.6264 E-2	40.219	240.924	0.8055	7.072	7.967	20.128	4.337
3.9888 E-2	39.699	245.999	0.7994	7.187	8.077	19.433	5.058
4.4578 E-2	39.094	253.566	0.7900	7.352	8.231	18.630	6.146
4.8425 E-2	38.686	261.185	0.7806	7.505	8.372	18.038	7.202
5.2327 E-2	38.393	270.963	0.7693	7.685	8.538	17.499	8.470
5.6264 E-2	38.281	283.993	0.7553	7.900	8.737	17.014	10.011
6.0219 E-2	38.458	302.074	0.7381	8.167	8.987	16.598	11.914
6.4183 E-2	39.116	328.489	0.7163	8.513	9.315	16.271	14.323
6.7163 E-2	40.154	357.685	0.6958	8.853	9.642	16.107	16.606
7.0154 E-2	42.051	401.652	0.6699	9.312	10.088	16.058	19.501
7.3174 E-2	45.719	476.253	0.6354	9.990	10.753	16.213	23.393
7.5226 E-2	50.492	566.654	0.6038	10.701	11.456	16.557	26.996
7.5959 E-2	53.162	615.840	0.5898	11.051	11.803	16.772	28.603

Table 3. Equation of state of the inner crust. First line corresponds to the neutron drip point, as calculated within the Compressible Liquid Drop Model. Last line corresponds to the bottom edge of the crust.

n_b (fm^{-3})	ρ (g cm^{-3})	P (erg cm^{-3})	Γ	n_b (fm^{-3})	ρ (g cm^{-3})	P (erg cm^{-3})	Γ
2.0905 E-4	3.4951 E11	6.2150 E29	1.177	9.9795 E-3	1.6774 E13	3.0720 E31	1.342
2.2059 E-4	3.6883 E11	6.4304 E29	0.527	1.2513 E-2	2.1042 E13	4.1574 E31	1.332
2.3114 E-4	3.8650 E11	6.5813 E29	0.476	1.6547 E-2	2.7844 E13	6.0234 E31	1.322
2.6426 E-4	4.4199 E11	6.9945 E29	0.447	2.1405 E-2	3.6043 E13	8.4613 E31	1.320
3.0533 E-4	5.1080 E11	7.4685 E29	0.466	2.4157 E-2	4.0688 E13	9.9286 E31	1.325
3.5331 E-4	5.9119 E11	8.0149 E29	0.504	2.7894 E-2	4.7001 E13	1.2023 E32	1.338
4.0764 E-4	6.8224 E11	8.6443 E29	0.554	3.1941 E-2	5.3843 E13	1.4430 E32	1.358
4.6800 E-4	7.8339 E11	9.3667 E29	0.610	3.6264 E-2	6.1153 E13	1.7175 E32	1.387
5.3414 E-4	8.9426 E11	1.0191 E30	0.668	3.9888 E-2	6.7284 E13	1.9626 E32	1.416
6.0594 E-4	1.0146 E12	1.1128 E30	0.726	4.4578 E-2	7.5224 E13	2.3024 E32	1.458
7.6608 E-4	1.2831 E12	1.3370 E30	0.840	4.8425 E-2	8.1738 E13	2.6018 E32	1.496
1.0471 E-3	1.7543 E12	1.7792 E30	0.987	5.2327 E-2	8.8350 E13	2.9261 E32	1.536
1.2616 E-3	2.1141 E12	2.1547 E30	1.067	5.6264 E-2	9.5022 E13	3.2756 E32	1.576
1.6246 E-3	2.7232 E12	2.8565 E30	1.160	6.0219 E-2	1.0173 E14	3.6505 E32	1.615
2.0384 E-3	3.4178 E12	3.7461 E30	1.227	6.4183 E-2	1.0845 E14	4.0509 E32	1.650
2.6726 E-3	4.4827 E12	5.2679 E30	1.286	6.7163 E-2	1.1351 E14	4.3681 E32	1.672
3.4064 E-3	5.7153 E12	7.2304 E30	1.322	7.0154 E-2	1.1859 E14	4.6998 E32	1.686
4.4746 E-3	7.5106 E12	1.0405 E31	1.344	7.3174 E-2	1.2372 E14	5.0462 E32	1.685
5.7260 E-3	9.6148 E12	1.4513 E31	1.353	7.5226 E-2	1.2720 E14	5.2856 E32	1.662
7.4963 E-3	1.2593 E13	2.0894 E31	1.351	7.5959 E-2	1.2845 E14	5.3739 E32	1.644

Table 4. Composition of the liquid core. Fractions of particles are defined as $x_j = n_j/n_b$. Neutron fraction can be calculated using $x_n = 1 - x_p$.

n_b (fm^{-3})	x_p (%)	x_e (%)	x_μ (%)	n_b (fm^{-3})	x_p (%)	x_e (%)	x_μ (%)
0.0771	3.516	3.516	0.000	0.490	7.516	4.960	2.556
0.0800	3.592	3.592	0.000	0.520	7.587	4.954	2.634
0.0850	3.717	3.717	0.000	0.550	7.660	4.952	2.708
0.0900	3.833	3.833	0.000	0.580	7.736	4.955	2.781
0.1000	4.046	4.046	0.000	0.610	7.818	4.964	2.854
0.1100	4.233	4.233	0.000	0.640	7.907	4.979	2.927
0.1200	4.403	4.398	0.005	0.670	8.003	5.001	3.002
0.1300	4.622	4.521	0.101	0.700	8.109	5.030	3.079
0.1600	5.270	4.760	0.510	0.750	8.309	5.094	3.215
0.1900	5.791	4.896	0.895	0.800	8.539	5.178	3.361
0.2200	6.192	4.973	1.219	0.850	8.803	5.284	3.519
0.2500	6.499	5.014	1.485	0.900	9.102	5.410	3.692
0.2800	6.736	5.031	1.705	0.950	9.437	5.557	3.880
0.3100	6.920	5.034	1.887	1.000	9.808	5.726	4.083
0.3400	7.066	5.026	2.040	1.100	10.663	6.124	4.539
0.3700	7.185	5.014	2.170	1.200	11.661	6.602	5.060
0.4000	7.283	4.999	2.283	1.300	12.794	7.151	5.643
0.4300	7.368	4.984	2.383	1.400	14.043	7.762	6.281
0.4600	7.444	4.971	2.473	1.500	15.389	8.424	6.965

Table 5. Equation of state of the liquid neutron-star core.

n_b (fm^{-3})	ρ (g cm^{-3})	P (erg cm^{-3})	Γ	n_b (fm^{-3})	ρ (g cm^{-3})	P (erg cm^{-3})	Γ
0.0771	1.3038 E14	5.3739 E32	2.159	0.4900	8.8509 E14	1.0315 E35	2.953
0.0800	1.3531 E14	5.8260 E32	2.217	0.5200	9.4695 E14	1.2289 E35	2.943
0.0850	1.4381 E14	6.6828 E32	2.309	0.5500	1.0102 E15	1.4491 E35	2.933
0.0900	1.5232 E14	7.6443 E32	2.394	0.5800	1.0748 E15	1.6930 E35	2.924
0.1000	1.6935 E14	9.9146 E32	2.539	0.6100	1.1408 E15	1.9616 E35	2.916
0.1100	1.8641 E14	1.2701 E33	2.655	0.6400	1.2085 E15	2.2559 E35	2.908
0.1200	2.0350 E14	1.6063 E33	2.708	0.6700	1.2777 E15	2.5769 E35	2.900
0.1300	2.2063 E14	1.9971 E33	2.746	0.7000	1.3486 E15	2.9255 E35	2.893
0.1600	2.7223 E14	3.5927 E33	2.905	0.7500	1.4706 E15	3.5702 E35	2.881
0.1900	3.2424 E14	5.9667 E33	2.990	0.8000	1.5977 E15	4.2981 E35	2.869
0.2200	3.7675 E14	9.2766 E33	3.025	0.8500	1.7302 E15	5.1129 E35	2.858
0.2500	4.2983 E14	1.3668 E34	3.035	0.9000	1.8683 E15	6.0183 E35	2.847
0.2800	4.8358 E14	1.9277 E34	3.032	0.9500	2.0123 E15	7.0176 E35	2.836
0.3100	5.3808 E14	2.6235 E34	3.023	1.0000	2.1624 E15	8.1139 E35	2.824
0.3400	5.9340 E14	3.4670 E34	3.012	1.1000	2.4820 E15	1.0609 E36	2.801
0.3700	6.4963 E14	4.4702 E34	2.999	1.2000	2.8289 E15	1.3524 E36	2.778
0.4000	7.0684 E14	5.6451 E34	2.987	1.3000	3.2048 E15	1.6876 E36	2.754
0.4300	7.6510 E14	7.0033 E34	2.975	1.4000	3.6113 E15	2.0679 E36	2.731
0.4600	8.2450 E14	8.5561 E34	2.964	1.5000	4.0498 E15	2.4947 E36	2.708

where we have used $p_{Fj} = \hbar(n_j/3\pi^2)^{1/3}$. The threshold density above which electron direct Urca process is allowed is 1.35 fm^{-3} , and that for the muon direct Urca process is somewhat higher, 1.44 fm^{-3} . The electron direct Urca threshold for our EOS is much higher than 0.78 fm^{-3} , obtained for the APR model. However, in contrast to proton fraction at $n_b \lesssim n_0$, our values of x_p at higher density should be taken with a grain of salt: this feature of our

model is based on an extrapolation from nuclear densities, and – in contrast to the EOS itself – it was not subjected to a reliable constraint.

The equation of state of the liquid core is given in Table 5. Its properties will be discussed in Sect. 5. Here we will restrict ourselves to a comment referring to its practical use in neutron star calculations. The tiny density jump between core and crust is not relevant for the

applications to calculations of the neutron star structure (although it can play a role in neutron star dynamics). One can remove the first line of Table 5 and then match the resulting EOS of the core to that of the inner crust, given in Table 3. However, one can also remove the last line of Table 3, and then match the EOS of the inner crust to that of the inner core, given in Table 5. In practice, the difference in neutron star structure, resulting from the difference in these two prescriptions, is negligibly small.

5. Properties of the EOS

Using the CLDM of dense matter, based on the SLy effective nucleon-nucleon interaction, we determined the EOS of cold neutron-star matter in the interval of density from 10^8 g cm^{-3} to $4 \times 10^{15} \text{ g cm}^{-3}$. This EOS is displayed in Fig. 1, where for the sake of clarity of presentation at higher density, the lower-density limit has been set at $10^{10} \text{ g cm}^{-3}$. Our EOS covers three main regions of neutron-star interior: outer crust, inner crust and liquid core. In the displayed region of the outer crust the EOS is well approximated by a polytrope, with nearly constant adiabatic index (see below). Just after neutron drip, the EOS softens considerably, gradually stiffens in the higher-density part of the inner crust and then stiffens considerably after crossing the crust-core interface.

5.1. Adiabatic index Γ

An important dimensionless parameter characterizing the stiffness of the EOS at given density is the adiabatic index, defined by

$$\Gamma = \frac{n_b}{P} \frac{dP}{dn_b} = \frac{\rho + P/c^2}{P} \frac{dP}{d\rho}. \quad (7)$$

The three main regions of the neutron star interior are characterized by distinct behavior of Γ , displayed in Fig. 2. Precise values of Γ are given in Tables 3 and 5. In the outer crust, the value of Γ depends quite weakly on density. It should be mentioned that a weak, smooth decrease of Γ in the higher-density part of the outer crust, displayed in Fig. 2, is an artifact of the CLDM of dense matter. Had we used a model of the outer crust, based on the A, Z table of nuclear masses (experimental where available, calculated using semi-empirical mass formula elsewhere), we would get a sequence of shells with fixed A, Z , and density jump at the neighboring shells interface (Baym et al. 1971b; for a recent calculation see Haensel & Pichon 1994). Above 10^8 g cm^{-3} , adiabatic index within each A, Z shell would be $\Gamma \simeq 4/3$. This can be easily understood, because the main component of the matter pressure comes from the ultrarelativistic electron gas, and the most important correction from Coulomb (lattice) term in the energy density, both of which behave as $\propto (Z\rho/A)^{4/3}$ (Baym et al. 1971b). Notice that for the outer crust ρ is to a very good approximation, proportional to n_b . In the CLDM, with continuous variables A, Z , density jumps do not appear, and decrease of Γ below $4/3$ results mostly from the monotonic, smooth

increase of A with increasing density. Actually, such a behavior within the CLDM simulates “averaging” of the value of Γ over the density jumps, which effectively softens (as first-order phase transitions between shells with different nuclides should do) the EOS of the outer crust.

Neutron drip at ρ_{ND} implies a dramatic drop in Γ , which corresponds to strong softening of the EOS. Density stays continuous at the neutron drip point, with low-density dripped neutrons contributing to n_b and ρ , but exerting a very small pressure, and moreover being in phase equilibrium with nuclear matter of nuclei. Consequently, Γ drops by more than a factor of two, a sizable part of this drop occurring via discontinuous drop at ρ_{ND} , characteristic of a second-order phase transition. After this initial dramatic drop, matter stiffens, because pressure of neutron gas increases. The actual value of Γ results from an interplay of several factors, with stiffening due to Fermi motion and neutron-neutron repulsion in dripped non-relativistic neutron gas and, countering this, softening Coulomb (lattice) contribution, a rather soft contribution of ultrarelativistic electron gas, and a softening effect of neutron gas – nuclear matter coexistence. As one sees in Fig. 2, Γ reaches the value of about 1.6 near the bottom edge of the inner crust, only slightly lower than $5/3$ characteristic of a non-relativistic free Fermi gas.

At the crust-core interface, matter strongly stiffens, and Γ increases discontinuously, by 0.5, to about 2.2. This jump results from the disappearance of nuclei: a two-phase nucleon system changes into a single-phase one, and repulsive nucleon-nucleon interaction is no longer countered by softening effects resulting from the presence of nuclear structure and neutron gas – nuclear matter phase coexistence. With increasing density, Γ grows above 3 at $2\rho_0$, due to increasing contribution of repulsive nucleon interactions.

A tiny notch appears at the muon threshold, at which Γ undergoes small, but clearly visible, discontinuous drop. It is due to the appearance of new fermions – muons, which replace high-energy electrons (electron Fermi energy $\mu_e \geq 105.7 \text{ MeV}$). Replacing rapidly moving electrons by slowly moving muons leads to a drop in the sound velocity (and Γ) just after the threshold. Because lepton contribution to pressure is at this density very small, the overall effect is small. A discontinuous drop in Γ at muon threshold is characteristic of a second-order phase transition at which density is continuous but compressibility is not.

At higher densities, $\rho > 2\rho_0$, Γ decreases slowly, which results from the interplay of the density dependence of nuclear interactions and of increasing proton fraction.

5.2. Deviations from beta-equilibrium and Γ_{fr}

The calculation of the EOS has been done under assumption of full thermodynamic equilibrium. Therefore, Γ determines the response of neutron star matter to a local change of density when this assumption is valid. In the case of middle aged or old neutron stars however, the

timescale of beta processes, which assure beta equilibrium expressed in Eq. (3), is many orders of magnitude longer than the characteristic timescales of dynamical phenomena, such as stellar pulsations or sound waves, excited in neutron star interior. In such a case, proton, electron and muon fractions in a perturbed element of neutron star matter cannot adjust to the instantaneous value of n_b because beta processes are too slow, and in practice the values of x_p , x_e , and x_μ can be considered as fixed at their unperturbed values. In view of this, the response of pressure to perturbation of density is determined by Γ_{fr} , calculated under the condition of constant composition (Gourgoulhon et al. 1995). Both adiabatic indices are related by

$$\Gamma = \Gamma_{\text{fr}} + \frac{n_b}{P} \sum_j \left(\frac{\partial P}{\partial x_j} \right)_{n_b} \left(\frac{\partial x_j}{\partial n_b} \right)_{\text{eq}}, \quad (8)$$

where the index “eq” indicates that the derivative has to be calculated assuming beta equilibrium (i.e., from the EOS), and “fr” indicates a constant (frozen) composition.

Both Γ and Γ_{fr} in the liquid interior are shown in Fig. 3. Freezing the composition stiffens neutron star matter, $\Gamma_{\text{fr}} > \Gamma$, the effect being of the order of a few percent. Another effect of the composition freezing is removing of a softening just after the appearance of muons, because of the slowness of processes in which they are produced or absorbed.

5.3. Velocity of sound and causality

The adiabatic sound speed is given by

$$v_s^2 = \left(\frac{\partial P}{\partial \rho} \right)_S, \quad (9)$$

where S is the entropy per baryon. The value of v_s may become comparable to c in dense neutron star core.

The characteristic period of sound waves excited in the liquid core can be estimated as $\tau_s \sim R/v_s \sim 0.1$ ms. Therefore, τ_s is much shorter than the timescale of beta processes, so that in this case

$$v_s = c \sqrt{\frac{\Gamma_{\text{fr}}}{\rho c^2 / P + 1}}. \quad (10)$$

A *necessary* condition for causality in a liquid medium is $v_s \leq c$: sound has to be *subluminal*. As our many-body model for the nucleon component of dense matter is non-relativistic, it is not obvious a priori that the EOS we have calculated respects this condition at high density. The calculation shows, that $v_s \leq c$ is valid for our EOS at all densities relevant for neutron stars (i.e., for $\rho < \rho_{\text{max}}$, see Sect. 6.1). It should be mentioned, however, that $v_s \leq c$ is not *sufficient* for causality to be respected by a neutron star matter model. Strict conditions for causality can be only derived using the kinetic theory, which describes all modes which can propagate in neutron star

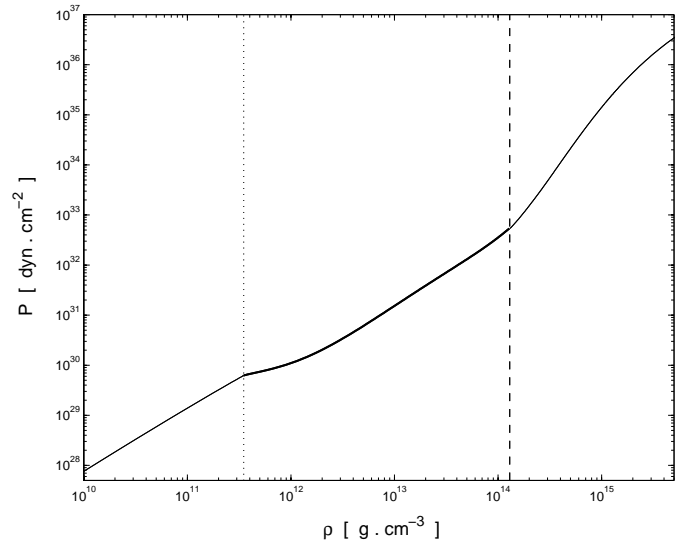


Fig. 1. The SLy EOS of the ground-state neutron star matter. Dotted vertical line corresponds to the neutron drip and the dashed one to the crust-liquid core interface.

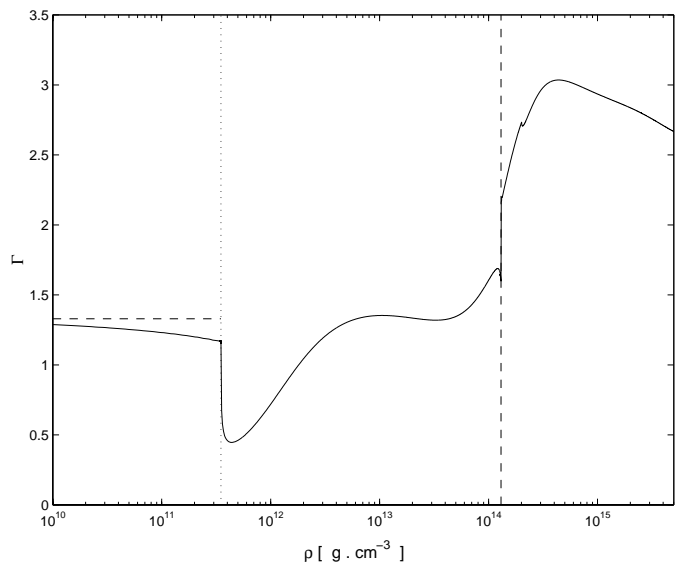
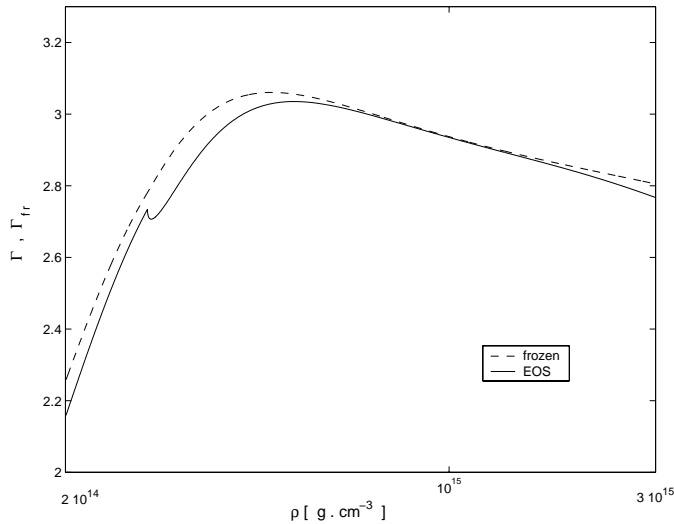


Fig. 2. Adiabatic index of the Sly EOS versus matter density. Matter is assumed to be in full thermodynamic equilibrium. Dotted vertical line: neutron drip. Dashed vertical line: crust – liquid core interface. Dashed horizontal line in the region of the outer crust is $\Gamma = 1.33$ obtained using empirical and semi-empirical (i.e., from mass formulae) masses of nuclei and removing the points corresponding to the density jumps between shells with different nuclei (Baym et al. 1971b; Haensel & Pichon 1994).

matter (Olson 2000). In a simplified case of a schematic (unrealistic) model of neutron star matter a set of conditions resulting from kinetic equations was obtained by Olson (2000). However, the problem of a complete set of causality conditions was not studied for realistic models of neutron star matter, and we will not attempt to solve this problem in the present paper.

Table 6. Configuration of maximum allowable mass for static neutron stars.

EOS	M [M_\odot]	R [km]	n_c [fm $^{-3}$]	ρ_c [10^{14} g/cm 3]	P_c [10^{36} dyn/cm 2]	A [10^{57}]	z_{surf}	E_{bind} [10^{53} erg]	I [10^{45} g cm 2]
SLy	2.05	9.99	1.21	2.86	1.38	2.91	0.594	6.79	1.91
FPS	1.80	9.27	1.46	3.40	1.37	2.52	0.531	5.37	1.36

**Fig. 3.** Adiabatic index of the SLy EOS of the liquid core. Solid line: beta equilibrium of $npe\mu$ matter (equilibrium composition during compression or decompression). Dashed line: vanishing rate of weak processes in $npe\mu$ matter (frozen composition during compression or decompression).

6. Neutron star structure. Static equilibrium configurations

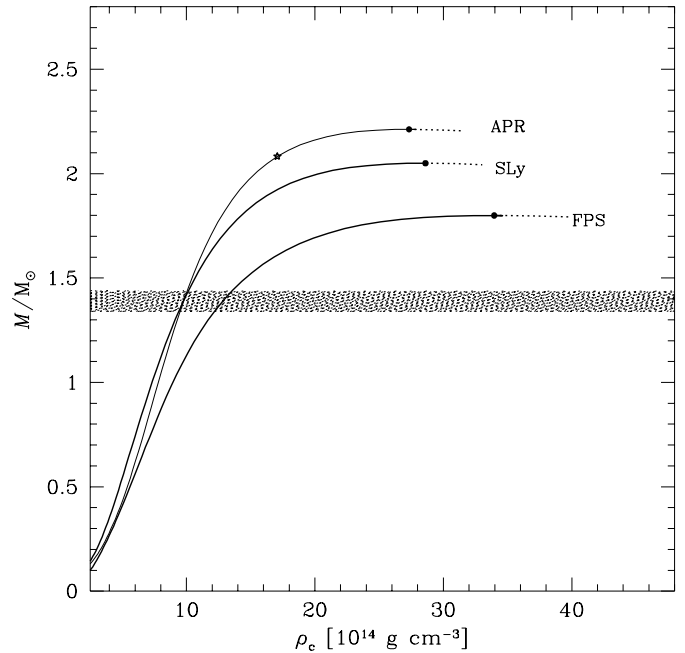
Configurations of hydrostatic equilibrium of non-rotating neutron stars have been calculated by solving the Tolman-Oppenheimer-Volkoff (TOV) equations

$$\begin{aligned} \frac{dP}{dr} &= -\frac{G\rho m}{r^2} \left(1 + \frac{P}{\rho c^2}\right) \left(1 + \frac{4\pi Pr^3}{mc^2}\right) \left(1 - \frac{2Gm}{rc^2}\right)^{-1}, \\ \frac{dm}{dr} &= 4\pi r^2 \rho, \end{aligned} \quad (11)$$

where r is the radial coordinate in the Schwarzschild metric. The TOV equations are supplemented with an equation determining number of baryons, a , within the sphere of radius r ,

$$\frac{da}{dr} = 4\pi r^2 n_b \left(1 - \frac{2Gm}{rc^2}\right)^{-\frac{1}{2}}. \quad (12)$$

Equations (11), (12) were integrated from the center of the configuration, with boundary condition at $r = 0$: $P(0) = P_c$, $m(0) = 0$, $a(0) = 0$. The stellar surface at $r = R$ was then determined from $P(R) = 0$. The total gravitational mass $M = m(R)$, and the total number of baryons $A = a(R)$.

**Fig. 4.** Gravitational mass M versus central density ρ_c , for the SLy, FPS, and APR EOS of dense matter. Maximum on the mass-central density curves is indicated by a filled circle. On the APR curve, configurations to the right of the asterisk contain a central core with $v_{\text{sound}} > c$. Configurations to the right of the maxima are unstable with respect to small radial perturbations, and are denoted by a dotted line. The shaded band corresponds to the range of precisely measured masses of binary radio pulsars.

Models of cold, static neutron stars form a one-parameter family. They can be labeled by their central pressure, P_c , or equivalently by their central density, ρ_c .

6.1. Mass, central density, and radius of neutron stars

In Fig. 4 we show dependence of gravitational mass on the central density, ρ_c , for $\rho_c > 3 \times 10^{14}$ g cm $^{-3}$, and compare it with that obtained for the FPS EOS. Actually, on the lower-density side the curve $M(\rho_c)$ exhibits a minimum at $M_{\text{min}} \simeq 0.09 M_\odot$, not shown in the figure. The value of M_{min} depends rather weakly on the EOS. On the higher-density side, $M(\rho_c)$ has a maximum. The existence of M_{max} (for any EOS) is an important consequence of general relativity. Configuration with $M > M_{\text{max}}$ cannot exist

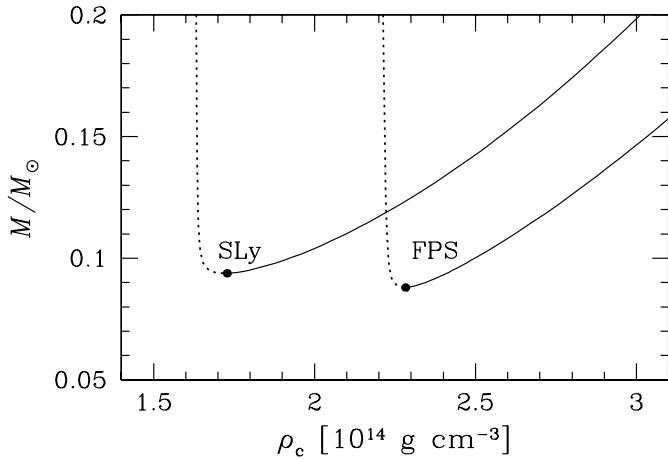


Fig. 5. Gravitational mass versus central density, in the vicinity of the minimum mass, for static neutron stars. Dotted lines – configurations unstable with respect to small radial perturbations. Minimum mass configuration is indicated by a filled circle.

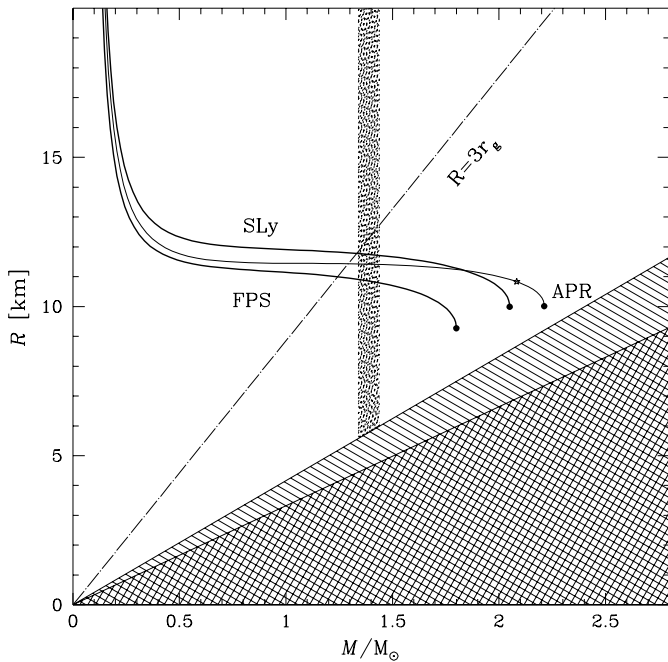


Fig. 6. Neutron star radius R versus gravitational mass M , with notation as in Fig. 4. Doubly hatched area is prohibited by general relativity, because it corresponds to $R < \frac{9}{8}r_g = 9GM/4c^2$ (for a general proof, see Weinberg 1972). All hatched triangle (double and single hatched) is prohibited by the general relativity and condition $v_{\text{sound}} < c$ (necessary but not sufficient for respecting causality, Olsson 2000) combined. The shaded band corresponds to the range of precisely measured masses of binary radio pulsars.

in hydrostatic equilibrium and collapse into black holes. We get $M_{\text{max}} = 2.05 M_{\odot}$, to be compared with $1.80 M_{\odot}$ for a softer FPS EOS.

Central density of the maximum allowable mass configuration is the maximum one which can be reached within static neutron stars. Models with $\rho_c > \rho_c(M_{\text{max}}) \equiv \rho_{\text{max}}$

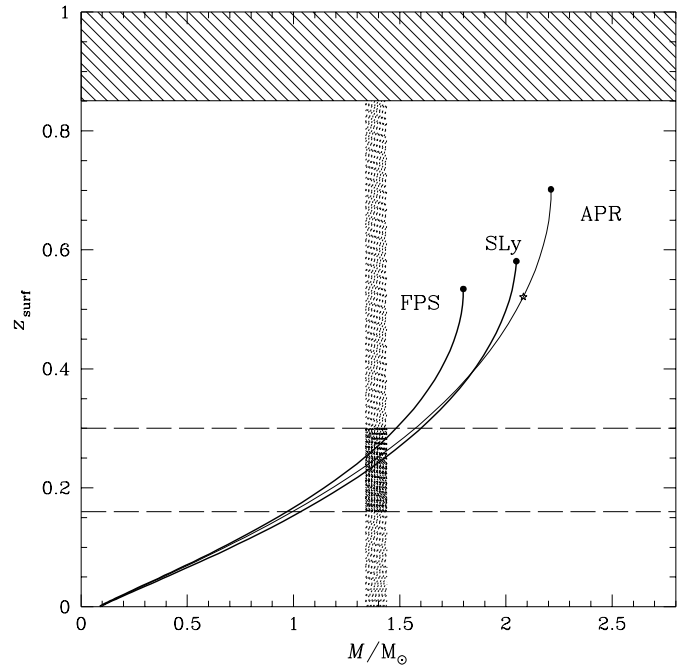


Fig. 7. Surface redshift z_{surf} versus gravitational mass M . Hatched area is prohibited for EOSs with $v_{\text{sound}} < c$. Shaded vertical band corresponds to the range of precisely measured masses of binary radio pulsars. The band limited by two dashed horizontal lines corresponds to the estimate of z_{surf} from the measured spectrum of the gamma-ray burst GB 790305b.

have $dM/d\rho_c < 0$. They are therefore unstable with respect to small radial perturbations and collapse into black holes (see, e.g., Shapiro & Teukolsky 1983). The maximum central density for static stable neutron stars is, for our EOS, $2.9 \times 10^{15} \text{ g cm}^{-3}$, to be compared with $3.4 \times 10^{15} \text{ g cm}^{-3}$ for the FPS EOS. Corresponding maximum value of baryon density is $n_{\text{max}} = 1.21 \text{ fm}^{-3} \simeq 7.6n_0$, to be compared with $1.46 \text{ fm}^{-3} \simeq 9.1n_0$ obtained for the FPS EOS. A complete set of parameters of configuration with maximum allowable mass for our EOS is presented in Table 6, where the corresponding parameters obtained for the FPS EOS are also given for comparison.

Comparison with the APR EOS is also of interest, and therefore we show the $M(\rho_c)$ curve for this EOS. The curve obtained for our EOS is quite close to the APR one, especially for $1 \leq M/M_{\odot} \lesssim 2$. It should be mentioned, that for $\rho_c > 1.73 \times 10^{15} \text{ g cm}^{-3}$ the APR neutron star models contain a central core with $v_{\text{sound}} > c$, and should therefore be taken with a grain of salt. Such a problem does not arise for our EOS, for which $v_{\text{sound}} < c$ within all stable neutron star models.

Precisely measured masses of radio pulsars in binaries with another neutron star span the range $1.34\text{--}1.44 M_{\odot}$ (Thorsett & Chakrabarty 1999), visualized in Fig. 4 by a shaded band. For neutron stars of such masses, central density is about $1 \times 10^{15} \text{ g cm}^{-3}$, slightly below $4\rho_0$; this result is nearly the same as for the APR EOS. For the FPS EOS, neutron star of such a mass has higher central density, about $1.3 \times 10^{15} \text{ g cm}^{-3} \simeq 5\rho_0$.

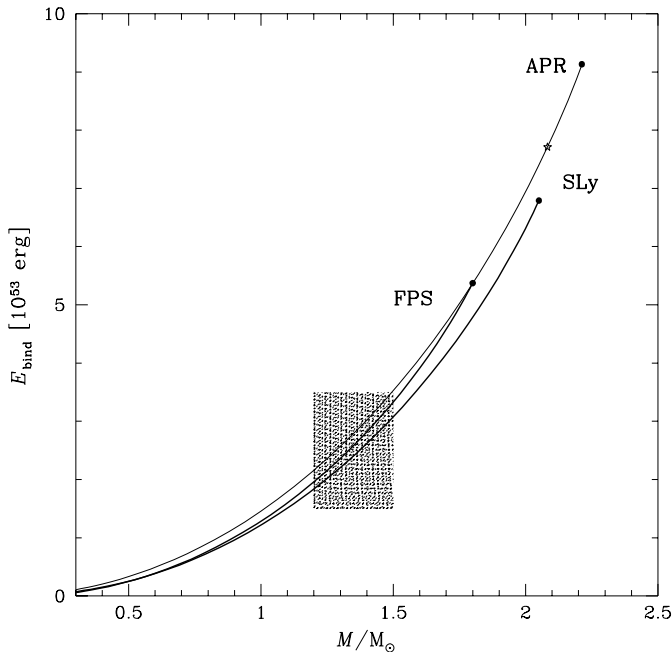


Fig. 8. Binding energy relative to dispersed ^{56}Fe versus gravitational mass. The shaded rectangle corresponds to the estimates of the total energy of the neutrino burst in SN 1987A, and to the estimates of the mass of neutron star formed in this event.

Table 7. Configurations of minimum mass for static neutron stars.

EOS	M_{\min} [M_{\odot}]	ρ_c [10^{14} g/cm 3]	R [km]	M_{core}/M	R_{core} [km]
SLy	0.094	1.6	270	0.02	3.8
FPS	0.088	2.2	220	0.03	4.2

6.2. Minimum mass of neutron stars

With decreasing value of the central density, the mass of equilibrium configuration decreases. Finally, one reaches the minimum, M_{\min} , on the $M - \rho_c$ curve. The curve $M(\rho_c)$ in the neighbourhood of M_{\min} is shown in Fig. 5. Parameters of the minimum mass configuration for static neutron stars are given in Table 7, where for the sake of comparison we show also corresponding values calculated for the FPS EOS.

The value of M_{\min} for the SLy EOS and the FPS EOS are quite similar: in both cases $M_{\min} \simeq 0.09 M_{\odot}$. Since the SLy EOS is stiffer than the FPS one in the vicinity of the crust-core interface, its M_{\min} configuration is less dense and has larger radius. In both cases it has a small central liquid core, containing 2% of mass in the case of the SLy EOS and 3% of star mass in the case of a softer FPS EOS.

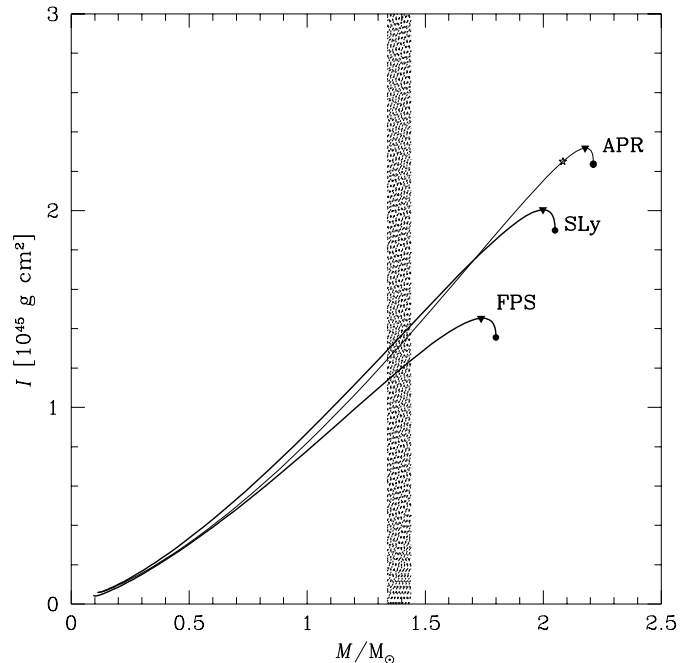


Fig. 9. Moment of inertia for slow, rigid rotation versus gravitational mass. The configuration with maximum I is indicated by a filled triangle, and that of maximum mass – by a filled circle. A shaded band corresponds to the range of precisely measured masses of binary radio pulsars.

6.3. Radius versus gravitational mass

The radius-mass relation, obtained for our EOS for static, cold neutron stars, is shown in Fig. 5, where for the sake of comparison we show also the $R(M)$ curve for the FPS EOS. For masses between $1 M_{\odot}$ and $M_{\max} = 2.05 M_{\odot}$, the neutron star radius decreases rather weakly with increasing mass, from 12 km to 10 km. For neutron star masses, measured for some binary radio pulsars (shaded band), the radius is slightly below 12 km. The insensitivity of R to M for $1 \lesssim M/M_{\odot} \lesssim M_{\max}$ is typical of the realistic EOS without a strong softening at high density. The reasons for such a weak dependence of R on M have been explained by Lattimer & Prakash (2001).

At the same value of M between $0.5 M_{\odot}$ and $1.5 M_{\odot}$, the radius of the SLy neutron star is some ~ 1 km larger than that obtained for the FPS EOS; the difference increases with increasing M , and reaches 2 km at $1.80 M_{\odot}$. It is of interest to compare $R(M)$ curve for our EOS also with that obtained for the APR EOS. For $1 \lesssim M/M_{\odot} \lesssim 2$ both curves are quite similar. Note that highest-mass segment (to the right of the asterisk) of the APR curve should be treated with caution, because stellar models contain there a central core with $v_{\text{sound}} > c$. It is due to this unphysical feature that the APR $R(M)$ curve approaches so closely the prohibited hatched region of the $R - M$ plane.

For a static neutron star, general relativity predicts that the circular Keplerian orbits (for test particles) with $r > 3r_g$ are stable, and those with $r < 3r_g$ are unstable, where the gravitational radius $r_g \equiv 2GM/c^2 = 2.95 M/M_{\odot}$ km (see, e.g., Shapiro & Teukolsky 1983).

The radius of the *marginally stable* orbit, which separates these two classes of orbits, is therefore $r_{\text{ms}} = 3r_g = 12.4 (M/1.4 M_\odot)$ km. As we see in Fig. 6, for $M \gtrsim 1.4 M_\odot$ we have $r_{\text{ms}} > R$, and therefore for such neutron stars the innermost stable circular orbit (ISCO) is separated from the stellar surface by a gap. A similar situation holds also for the FPS EOS. Note that the existence of a gap between the ISCO and neutron star surface might be important for the interpretation of the spectra of the kilohertz Quasi Periodic Oscillations observed in the X-ray radiation of some Low Mass X-ray Binaries (van der Klis 2000).

6.4. Surface redshift

The surface redshift of photons emitted from neutron star photosphere is given by

$$z_{\text{surf}} = \left(1 - \frac{r_g}{R}\right)^{-\frac{1}{2}} - 1. \quad (13)$$

Surface redshift versus gravitational mass is plotted in Fig. 7. At given M , the SLy value of z_{surf} is systematically lower than for softer FPS EOS. However, the maximum surface redshift for the SLy EOS, 0.59, is some 10% higher than for the FPS EOS, 0.53. The larger value of M_{max} for stiffer SLy EOS plays a decisive role in determining the spacetime curvature close to neutron star with maximum allowable mass. In the range of measured values of masses of binary pulsars we get $z_{\text{surf}} \simeq 0.22 \div 0.26$, slightly higher than for the FPS EOS.

For $M \lesssim 2 M_\odot$, the $z_{\text{surf}}(M)$ curve for our EOS is quite similar to the APR one.

6.5. Binding energy

The binding energy of neutron star, E_{bind} , is defined as the mass defect with respect to a dispersed configuration of matter consisting of the same number of baryons, multiplied by c^2 . A dispersed configuration is characterized by negligible pressure and negligible gravitational interactions. Equivalently, one may define E_{bind} as a net work, needed to transform a neutron star into a dispersed configuration of matter. In what follows, we will use standard definition of E_{bind} , i.e., with respect to a dispersed configuration of a pressureless cloud of ^{56}Fe dust, with mass per nucleon $m_{\text{Fe}} \equiv \text{mass of } ^{56}\text{Fe atom}/56 = 1.6587 \times 10^{-24}$ g. Therefore,

$$E_{\text{bind}} = (Am_{\text{Fe}} - M)c^2. \quad (14)$$

With such a definition, E_{bind} represents a good approximation of the binding energy of neutron star with respect to the configuration of a presupernova core from which the neutron star was formed, via gravitational collapse, as a by-product of the type II supernova explosion. Binding energy is plotted versus M in Fig. 7. A given M , it is somewhat smaller than for a softer FPS EOS. However, the maximum value of E_{bind} , reached for M_{max} , is significantly larger for the SLy EOS than for a softer FPS

one. Binding of the neutron star is due to gravitational forces and it rises rapidly with M . Significantly larger value of M_{max} (by 10%), combined with approximate scaling $E_{\text{bind}} \propto M^2$ (Lattimer & Yahil 1989), explain why maximum binding energy for our SLy model is some 20% higher than for the FPS one.

The scaling argument is much less precise in the case of comparison of maximum E_{bind} for our EOS with the APR one. However, let us remind that the APR curve above the asterisk should be treated with caution.

For measured masses of binary pulsars, we get for our EOS $E_{\text{bind}} = 2.3 \div 2.7 \times 10^{53}$ erg; corresponding values for the FPS EOS are some 2×10^{52} erg higher.

6.6. Moment of inertia

Most observed neutron stars are rotating. However, even for most rapid millisecond pulsar PSR 1937+21, with rotation period $P_{\text{min}}^{\text{obs}} = 1.558$ ms, and angular frequency $\Omega_{\text{max}}^{\text{obs}} = 2\pi/\text{period} = 4033$ Hz, rotation implies only small changes of stellar structure for neutron stars with $M > 1 M_\odot$. Therefore, for the description of effects of rotation for observed neutron stars one can use *slow rotation* approximation, in which effects of rotation (assumed to be rigid) are treated using a lowest order perturbative scheme (Hartle 1967). In this approach, one calculates, in the linear approximation in the angular frequency as measured by a distant observer, Ω , total angular momentum of neutron star, $J \propto \Omega$ (next order term is cubic in Ω). Then, one gets *moment of inertia for slow, rigid rotation* as $I = J/\Omega$. Notice that within the slow rotation approximation I is independent of Ω and can be calculated from the structure of a non-rotating configuration of neutron star. The values of I are plotted, versus M , in Fig. 8. At given M , the value of I for our EOS is significantly higher than for softer FPS EOS. The difference rises rapidly with increasing M . An even larger difference is noted for the maximum value of the moment of inertia, I_{max} , reached for a mass slightly lower than M_{max} . Indeed, I_{max} depends quite sensitively on the stiffness of the EOS of dense matter, and this dependence can be approximated by $I_{\text{max}}/10^{45} \text{ g cm}^2 \simeq (M_{\text{max}}/M_\odot)(R_{M_{\text{max}}}/10 \text{ km})^2$ (Haensel 1990). As we noted before, M_{max} , and the radius at M_{max} , denoted by $R_{M_{\text{max}}}$, for the FPS EOS constitute, respectively, 88% and 93% of the values obtained for our SLy EOS. The simple approximate relation mentioned before, derived in (Haensel 1990), implies then that I_{max} for the FPS EOS has to be only 76% of I_{max} obtained with our EOS, which nicely reproduces results of exact calculations. The same scaling argument can be applied to “explain” the difference in I_{max} for our EOS and the APR one, in terms of the difference in M_{max} and $R_{M_{\text{max}}}$.

6.7. Effects of rotation at $P \geq 1.558$ ms

As we mentioned in the preceding subsection, the effect of rotation on the structure of neutron stars with $M > 1 M_\odot$

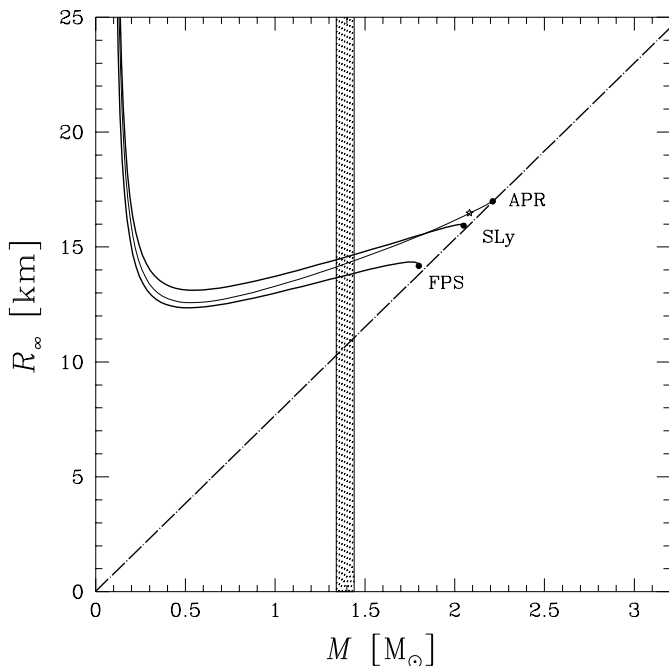


Fig. 10. Apparent radius of neutron star, R_∞ , versus gravitational mass, M , Long-dash-dot straight line corresponds to minimum R_∞ at a given M (see the text).

is small, and can be treated as a perturbation. Rigid rotation increases the maximum mass of the SLy neutron stars by less than two percent. The smallness of this effect is readily understood, because it is quadratic in a dimensionless parameter $\bar{\Omega} = \Omega/\sqrt{GM/R^3}$ (Hartle 1967). At present $P \geq 1.558$ ms, and therefore $\bar{\Omega}^2 \leq \bar{\Omega}_{\max}^{\text{obs}} = 0.06$ at M_{\max} for the SLy EOS. Now, maximal rotation, at $\Omega_{\max} \sim \sqrt{GM/R^3}$, implies increase of M_{\max} by about 20% (see next subsection). Therefore, fractional increase of M_{\max} connected with $\bar{\Omega}^2 \ll 1$ is $0.2\bar{\Omega}^2 < 2\%$.

However, $\bar{\Omega}_{\max}^{\text{obs}}$ increases with decreasing neutron star mass, and rotational effects at $P_{\min}^{\text{obs}} = 1.558$ ms become decisive for low-mass neutron stars. Namely, low-mass neutron stars become significantly flattened and because of a strongly increasing radius (with decreasing mass) they approach rapidly the *mass shedding limit*, at which the gravitational pull at the equator is exactly balanced by the centrifugal force. Exact 2-D calculation show that the minimum mass of neutron stars rotating rigidly at the minimum observed pulsar period of 1.558 ms is, for our EOS, $M_{\min}(1.558 \text{ ms}) = 0.61 M_\odot$, some seven times higher than for static neutron stars (Haensel et al. 2001).

6.8. Maximally rotating neutron star models

The minimum rotation period for rigidly rotating neutron stars, stable with respect to the axisymmetric perturbations, was calculated using the 2-D general relativistic code, based on the pseudospectral method for solving partial differential equation (Gourgoulhon et al., in

preparation). We get $P_{\min} = 0.55$ ms. For subluminal EOS ($v_s \leq c$), the values of P_{\min} can be estimated, with a good (a few percent) precision, using an “empirical formula” $P_{\min}/\text{ms} = 0.82 \cdot (M_{\max}/M_\odot)^{-1/2} (R_{M_{\max}}/10 \text{ km})^{3/2}$, where M_{\max} and $R_{M_{\max}}$ are mass and radius of *static* configuration with maximum allowable mass (Haensel & Zdunik 1989; Haensel et al. 1995). This empirical formula yields $P_{\min} \simeq 0.57$ ms, which is only 4% higher than the exact result. Using the empirical formula, one gets for the APR EOS the value of P_{\min} which is a few percent lower than for our EOS.

The maximum mass for rigidly rotating neutron stars is $M_{\max}^{\text{rot}} = 2.42 M_\odot$, 18% higher than the maximum mass for static configurations. For the FPS EOS, one obtains $M_{\max}^{\text{rot}} = 1.95 M_\odot$ (Cook et al. 1994), also 18% higher than for the static configuration. Such an increase of M_{\max} due to a maximal uniform rotation is characteristic of subluminal realistic baryonic EOS (Lasota et al. 1996).

7. Neutron star models vs. observations

7.1. Masses

The value of $M_{\max} = 2.05 M_\odot$ is sufficiently high to be consistent with measured masses of binary radio pulsars and with estimates of masses of X-ray pulsars and X-ray bursters. It is a little too low (by a few percent) to explain the upper-peak frequency 1.06 ± 0.02 kHz of the QPOs in 4U 1820-30 via the orbital motion of plasma clumps in the marginally stable circular orbit, which would require $M > 2.1 M_\odot$. However, the last constraint may be not valid because of doubts connected with interpretation of the kHz QPOs in this and other LMXBs. These doubts result from observed changes of the difference between the upper and lower peak frequencies, which within the beat-frequency model (Miller et al. 1998 and references therein) is identified with rotation frequency of neutron star, and should therefore be constant, apart from slight increase due to the accretion spin-up.

7.2. Apparent radii of isolated closeby neutron stars

Measuring the spectrum of photons emitted from the surface of a solitary neutron star, combined with knowledge of distance (from the annual parallax) enables one, in principle, to determine total photon luminosity, effective surface temperature and *apparent radius* of neutron star. Recently, such studies have been carried out for Geminga (Golden & Shearer 1999) and RX J185635-3754 (Walter 2001; Pons et al. 2001).

The apparent (or radiation) radius, measured by a distant observer, R_∞ , is related to R by

$$R_\infty = \frac{R}{\sqrt{1 - r_g/R}} = (1 + z_{\text{surf}})R. \quad (15)$$

The values of R_∞ versus M are plotted in Fig. 10. The $R_\infty(M)$ plot is very different from the $R(M)$ one (Haensel 2001). In particular, $R_\infty(M_{\max})$ is not the minimum value

of R_∞ ; the minimum is usually reached at $M \sim 0.5 M_\odot$, and for our EOS is 13.1 km, to be compared with slightly smaller minimum values of 12.3 km and 12.5 km for the FPS and APR EOS.

A strict lower bound on R_∞ at a given M results from the very definition of R_∞ , and does not depend on any physical constraint: $R_\infty(M) > R_{\infty,\min} = 7.66 (M/M_\odot)$ km (Lattimer & Prakash 2001, see also Haensel 2001). As one sees in Fig. 10, the values of R_∞ at M_{\max} are extremely close (within less than 1%) to $R_{\infty,\min}$. This property has been explained in (Haensel 2001).

The central value of R_∞ for Geminga, obtained by Golden & Shearer (1999) using the best-fit model atmosphere spectra, cannot be explained by our EOS, and actually – *by none* of existing baryonic EOS of dense matter (it could be modeled by a small mass strange star covered by a normal matter layer, to produce the observed photon spectrum). However, the uncertainty in the extracted value of R_∞ is large: it stems mainly from the uncertainty in the distance to Geminga (assumed to be $d = 159$ pc), but a poor knowledge of the photon spectrum plays also an important role. One therefore might argue, that because of these uncertainties the measured value of R_∞ cannot exclude our and other baryonic EOS of dense matter at a reasonably high confidence level of 95%.

In the case of RX J185635-3754 contradiction between extracted value of R_∞ , and theoretical models of neutron stars based on our EOS (and on other available models of dense matter) is even more dramatic (Pons et al. 2001)². The central best-fit value of R_∞ is 8.2 km (Fe atmosphere) and 7.8 km (Si-ash atmosphere), at assumed distance $d = 61$ pc. Non-uniformity of surface temperature, consistent with observational constraints, does not allow to remove this conflict between theory and observations. Unfortunately, proper inclusion of effects of surface magnetic field is not possible because of non-availability of magnetized heavy-metal atmosphere models (Pons et al. 2001). One may only hope, that the problem of the conflict between theoretical and measured R_∞ of closeby isolated neutron stars will be solved in the future studies.

Very recently, Rutledge et al. (2001) proposed a method of measuring R_∞ of neutron stars, observed as X-transients in globular clusters. They studied transient X-ray source CXOU 132619.7-472910.8 in NGC 5139. Fitting its photon spectrum with H-atmosphere model, they obtained, at 90% confidence level, $R_\infty = 14.3 \pm 2.5$ km, which is consistent with our EOS, and with FPS, APR and many other available EOS of dense matter. This method of measuring R_∞ seems to be very promising, because both distance and interstellar hydrogen column density are relatively well known for globular clusters.

² Low-mass strange quark stars covered with a thin normal matter envelope are excluded too because the best-fit redshift $z_{\text{surf}} \simeq 0.3-0.4$ (Pons et al. 2001).

7.3. Surface redshift

As of this writing (June 2001), the only reliable evaluation of z_{surf} seems to be connected with extraordinary gamma-ray burst GRB 790305b (of March 5th, 1979) from the soft-gamma repeater SGR 0526-66 associated with supernova remnant N49 in Large Magellanic Cloud. The spectrum of this gamma-ray burst exhibited a prominent emission line at 430 ± 30 keV, with full width at half-minimum $\simeq 150$ keV (Mazets et al. 1981, 1982). Assuming that the line originated from $e^+e^- \rightarrow 2\gamma$, and that line broadening resulted from the thermal motion in the plasma, one gets, after taking due account of the thermal blueshift (see, e.g., Higdon & Lingenfelder 1990), $z_{\text{surf}} = 0.23 \pm 0.07$. As one sees in Fig. 7, such surface redshift is predicted for neutron stars of $M = 1 \div 1.6 M_\odot$, while the central measured value of 0.23 corresponds for our EOS to a neutron star with $M \simeq 1.4 M_\odot$.

7.4. Binding energy and SN 1987A

The appearance of SN1987A in the UV and optical domain was preceded by a burst of neutrinos, detected on the Earth by neutrino detectors. The total of 25 events of the absorption of $\bar{\nu}_e$ on protons were registered within ~ 10 s. Analysis of these events, combined with: knowledge of detectors properties, assumption of spherical symmetry, knowledge of the distance to Large Magellanic Cloud, and basic features of the SN II theory, enabled the evaluation of the total energy of the neutrino burst as $E_\nu \simeq (2.5 \pm 1) \times 10^{53}$ erg (Lattimer & Yahil 1989). As about 99% of the total energy release in a SN II explosion is emitted in a neutrino burst, this was actually the measurement of the binding energy of a newly born neutron star, $E_{\text{bind}} \simeq E_\nu$. Stellar evolution theory tells us, that the neutron star born in SN1987A had $M = 1.2 \div 1.5 M_\odot$. This restricts the area in the $E_{\text{bind}} - M$ plane in Fig. 8 to a small shaded rectangle. This rectangle is nicely consistent with binding energies of neutron stars predicted by our EOS.

7.5. Crustal moment of inertia and pulsar glitches

It is widely believed that sudden spin ups of radio pulsars, called *glitches*, are due to the angular momentum transfer from a specific, weakly coupled to the rest of the star, superfluid component (dripped neutrons in the inner crust) – to the rest of the neutron star body (lattice of nuclei in the crust plus the liquid core) (Alpar et al. 1984). Since the discovery of glitches in 1969, more than thirty of them have been observed. Particularly large number of glitches have been detected in the timing of the Vela pulsar (thirteen during the period 1969–1999). The set of data on the Vela glitches was used by Link et al. (1999) to derive a constraint on the neutron star crustal moment of inertia, $I_{\text{crust}}/I > 1.4\%$. This constraint is satisfied by our EOS, provided the neutron star mass is below $1.75 M_\odot$. Let us mention that in the case of a softer FPS EOS neutron star

mass should not exceed $1.6 M_{\odot}$ in order to satisfy this constraint.

7.6. Neutron star cooling

For our specific SLy model, the threshold density for the direct electron Urca process, 1.35 fm^{-3} , is above the maximum central density of neutron stars. Taken at its face value, this would mean that the SLy model does not allow for the direct Urca process involving nucleons in neutron stars. One should keep in mind however, that the specific SLy4 model that we used is only one of a larger set of the SLy family. We remind that for some versions of these effective nuclear interactions direct Urca process was allowed in massive neutron stars (see Chabanat et al. 1997). Moreover, the SLy forces were constructed to reproduce best variational calculations for high density pure *neutron matter* with realistic neutron-neutron potentials, and therefore proton fraction they yield should not be considered at the same footing as the EOS for neutron star matter, in which protons play a rather small role.

8. Summary and conclusion

We calculated the EOS of neutron star matter, which describes in a physically unified way both the crust and the liquid core. The EOS, valid from 10^8 g cm^{-3} up to the maximum density reachable within neutron stars, was based on the recently derived SLy effective nucleon-nucleon interaction, which, due to its construction method, is particularly suitable for the description of strong interactions in the nucleon component of dense neutron star matter. Calculations were done assuming ground state of neutron star crust, and the “minimal” $n\text{pe}\mu$ composition of the liquid core. The minimum and maximum mass of non-rotating neutron stars are $0.09 M_{\odot}$ and $2.05 M_{\odot}$ respectively. Rigid rotation at the minimum observed pulsar period 1.558 ms increases the maximum mass by only about 1%, but effect on the minimum mass is large: it increases up to $0.61 M_{\odot}$.

Our model of matter at supranuclear densities is the simplest possible, and is based on experimental nuclear physics and relatively precise many-body calculations of dense neutron matter. We did not consider possible dense matter constituents, for which strong interactions are poorly known (hyperons), or which are hypothetical (pion and kaon condensates, quark matter). Such a model as that proposed in the present paper may seem very simple – as compared to a rich spectrum of possibilities considered in the literature on the constitution of dense neutron star cores. However, it has the virtue of giving a unified description of all the interior of a neutron star, and is firmly based on the most solid sector of our knowledge of nuclear interactions.

Acknowledgements. We express our gratitude to A. Potekhin for reading the manuscript, and for remarks and comments which helped to improve the present paper. We are also

grateful to him for his precious help in the preparation of figures. This research was partially supported by the KBN grant No. 5P03D.020.20 and by the CNRS/PAN Jumelage Astrophysique Program.

References

- Akmal, A., Pandharipande, V. R., & Ravenhall, D. G. 1998, *Phys. Rev. C*, 58, 1804
- Alpar, M. A., Langer, S. A., & Sauls, J. A. 1984, *ApJ*, 282, 533
- Baym, G., Bethe, H. A., & Pethick, C. J. 1971a, *Nucl. Phys. A*, 175, 225
- Baym, G., Pethick, C., & Sutherland, P. 1971b, *ApJ*, 170, 299
- Chabanat, E., Bonche, P., Haensel, P., Meyer, J., & Schaeffer, R. 1997, *Nucl. Phys. A*, 627, 710
- Chabanat, E., Bonche, P., Haensel, P., Meyer, J., & Schaeffer, R. 1998, *Nucl. Phys. A*, 635, 231
- Cheng, K. S., Yao, C. C., & Dai, Z. G. 1997, *Phys. Rev. C*, 55, 2092
- Cook, G. B., Shapiro, S. L., & Teukolsky, S. A. 1994, *ApJ*, 424, 823
- Douchin, F. 1999, Ph.D. Thesis, École Normale Supérieure de Lyon
- Douchin, F., Haensel, P., & Meyer, J. 2000, *Nucl. Phys. A*, 665, 419
- Douchin, F., & Haensel, P. 2000, *Phys. Lett. B*, 485, 107
- Golden, A., & Shearer, A. 1999, *A&A*, 342, L5
- Gourgoulhon, E., Haensel, P., & Gondek, D. 1995, *A&A*, 294, 747
- Friedman, B., & Pandharipande, V. R. 1981, *Nucl. Phys. A*, 361, 502
- Haensel, P. 2001, *A&A*, 380, 186
- Haensel, P., & Pichon, B. 1994, *A&A*, 283, 313
- Haensel, P., & Zdunik, J. L. 1989, *Nature*, 340, 617
- Haensel, P., Salgado, M., & Bonazzola, S. 1995, *A&A*, 296, 745
- Haensel, P., Zdunik, J. L., & Douchin, F. 2001, submitted
- Hartle, J. R. 1967, *ApJ*, 150, 1005
- Heiselberg, H., & Pandharipande, V. R. 2000, *Ann. Rev. Nucl. Part. Sci.*, 50, 481
- Higdon, J. M., & Lingenfelder, R. E. 1990, *ARA&A*, 28, 401
- van der Klis, M. 2000, *ARA&A*, 38, 717
- Kluźniak, W. 1998, *ApJ*, 509, L37
- Kutschera, M., & Wójcik, W. 1994, *Phys. Lett. B*, 325, 271
- Lasota, J.-P., Haensel, P., & Abramowicz, M. A. 1996, *ApJ*, 456, 300
- Lattimer, J. M., & Prakash, M. 2001, *ApJ*, 550, 426
- Lattimer, J. M., & Ravenhall, D. G. 1978, *ApJ*, 223, 314
- Lattimer, J. M., & Yahil, A. 1989, *ApJ*, 340, 426
- Lattimer, J. M., Pethick, C. J., Prakash, M., & Haensel, P. 1991, *Phys. Rev. Lett.*, 66, 2701
- Link, B., & Epstein, R. I. 1999, *Phys. Rev. Lett.*, 83, 3362
- Lorenz, C. P. 1991, Ph.D. Thesis, University of Illinois at Urbana-Champaign (unpublished)
- Lorenz, C. P., Ravenhall, D. G., & Pethick, C. J. 1993, *Phys. Rev. Lett.*, 70, 379
- Mazets, E. P., Golenetskii, S. V., Aptekar, R. L., Guryan, Ya. A., & Il'inskii, V. N. 1981, *Nature*, 290, 378
- Mazets, E. P., Golenetskii, S. V., Guryan, Ya. A., & Il'inskii, V. N. 1982, *ASS*, 84, 13
- Miller, M. C., Lamb, F. K., & Psaltis, D. 1998, *ApJ*, 508, 791
- Negele, J. W., & Vautherin, D. 1973, *Nucl. Phys. A*, 207, 298
- Olson, T. S. 2000, *Phys. Rev. C*, 63, 015802

- Oppenheimer, J. R., & Volkoff, G. M. 1939, *Phys. Rev.*, 55, 374
- Oyamatsu, K. 1993, *Nucl. Phys. A*, 561, 431
- Pandharipande, V. R., & Ravenhall, D. G. 1989, in *Proc. NATO Advanced Research Workshop on nuclear matter and heavy ion collisions, Les Houches, 1989*, ed. M. Soyeur et al. (Plenum, New York, 1989), 103
- Pethick, C. J., & Ravenhall, D. G. 1995, *Ann. Rev. Nucl. Part. Sci.*, 45, 429
- Pethick, C. J., Ravenhall, D. G., & Lorenz, C. P. 1995, *Nucl. Phys. A*, 584, 675
- Pons, J. A., Walter, F. M., Lattimer, J. M., et al. 2001, *ApJ*, submitted [[astro-ph/0107404](#)]
- Ravenhall, D. G., Bennett, C. D., & Pethick, C. J. 1972, *Phys. Rev. Lett.*, 28, 978
- Shapiro, S. L., & Teukolsky, S. A. 1983, *Black Holes, White Dwarfs and Neutron Stars* (Wiley, New York)
- Siemens, P. J., & Pandharipande, V. R. 1971, *Nucl. Phys. A*, 173, 561
- Sumiyoshi, K., Oyamatsu, K., & Toki, H. 1995, *Nucl. Phys. A*, 595, 327
- Thorsett, S. E., & Chakrabarty, D. 1999, *ApJ*, 512, 288
- Vautherin, D., & Brink, D. M. 1970, *Phys. Lett. B*, 32, 149
- Walter, F. M. 2001, *ApJ*, 549, 433
- Weinberg, S., *Gravitation and Cosmology: principles and applications of the general theory of relativity* (Wiley, New York)
- Wiringa, R. B., Fiks, V., & Fabrocini, A. 1988, *Phys. Rev. C*, 38, 1010
- Yakovlev, D. G., & Kaminker, A. D. 1994, in *The Equation of State in Astrophysics*, ed. G. Chabrier, & E. Schatzman (Cambridge U. Press), 214
- Zhang, W., Strohmayer, T. E., & Swank, J. H. 1997, *ApJ*, 481, L167